Targeting the IGF-Axis Potentiates Immunotherapy for Pancreatic Ductal Adenocarcinoma Liver Metastases by Altering the Immunosuppressive Microenvironment

Masakazu Hashimoto[1], John David Konda[1], Stephanie Perrino[1], Maria Celia Fernandez[1], Andrew M. Lowy[2], and Pnina Brodt[1,3,4]

ABSTRACT

Pancreatic ductal adenocarcinoma (PDAC) is a highly aggressive malignancy, resistant to chemotherapy and associated with high incidence of liver metastases and poor prognosis. Using murine models of aggressive PDAC, we show here that in mice bearing hepatic metastases, treatment with the IGF-Trap, an inhibitor of type I insulin-like growth factor receptor (IGF-IR) signaling, profoundly altered the local, immunosuppressive tumor microenvironment in the liver, curtailing the recruitment of myeloid-derived suppressor cells, reversing innate immune cell polarization and inhibiting metastatic expansion. Significantly, we found that immunotherapy with anti–PD-1 antibodies also reduced the growth of experimental PDAC liver metastases, and this effect was enhanced when combined with IGF-Trap treatment, resulting in further potentiation of a T-cell response. Our results show that a combinatorial immunotherapy based on dual targeting of the prometastatic immune microenvironment of the liver via IGF blockade, on one hand, and reversing T-cell exhaustion on the other, can provide a significant therapeutic benefit in the management of PDAC metastases.

Introduction

Pancreatic ductal adenocarcinoma (PDAC) is currently the fourth leading cause of cancer-related deaths in the industrialized world (1, 2). Despite remarkable advances in current diagnostic techniques (3), it has been widely reported that PDAC may surpass colorectal cancer to become the second leading cause of cancer-related death in the United States by 2030 (4). There is a dearth of effective therapies for pancreatic cancer and the 5-year survival still stands at 5% to 9%, the lowest of any common malignancy, identifying this disease as an obvious "unmet need" (5, 6). The most notable clinical features of PDAC are its propensity for aggressive local invasion, metastasis (mainly to the liver) and inherent resistance to conventional therapies. While approximately 50% of patients with pancreatic cancer present with evidence of distant disease, particularly in the liver, the remaining patients have localized disease without detectable metastases. Of these, 15% to 20% of patients are operable and therefore potentially amenable to curative therapy, while approximately 30% have locally advanced disease. The poor prognosis associated with pancreatic cancer is related mainly to the high incidence of synchronous liver metastases and postoperative recurrence (7). The liver is the major site of recurrent disease (8–10). Chemotherapy with gemcitabine or 5-fluorouracil, irinotecan and oxaliplatin (FOLFIRINOX) is still the standard of care for metastatic pancreatic cancer, but it is associated with high toxicity and limited survival advantage (10, 11). Thus, therapies that can effectively reduce the incidence of pancreatic cancer liver metastases and/or metastatic outgrowth would have tremendous potential to significantly improve survival.

Recent advances in targeting immune checkpoints such as programmed cell death-1 (PD-1) and CTL antigen-4 (CTLA-4) have yielded promising therapeutic results in several aggressive and treatment-refractory cancers such as malignant melanoma, small cell lung cancer and renal cell carcinoma (12–14). However, to date, immunotherapy has failed to show promise in the treatment of PDAC (15, 16). This, despite compelling clinical evidence for an effector T-cell infiltrate in PDAC, that, when present, has positive prognostic implications and can become reactive to the autologous tumors when further potentiated *ex vivo* (17). This failure of immunotherapy to alter the course of PDAC may be due, at least in part, to the presence of immunosuppressive cells such as myeloid-derived suppressor cells (MDSC) and tumor-associated macrophages (TAM) that polarize to an immunosuppressive M2 phenotype in the tumor microenvironment (TME) and impede T cell–mediated cytotoxicity, as well as promote PDAC progression through the release of proangiogenic and proinvasive factors such as VEGF and matrix metalloproteinases (MMP). Thus, therapeutic approaches that can co-target the immunosuppressive TME of PDAC, while also reversing T-cell exhaustion could enhance the efficacy of immunotherapy and are currently being sought (16, 18) (reviewed in ref. 19).

There is compelling experimental and clinicopathologic evidence that the insulin-like growth factor (IGF) axis plays an important role in PDAC progression (20–22). A recent analysis of surgical PDAC

[1]Department of Surgery, McGill University and the Cancer Program of the Research Institute of the McGill University Health Center, Montreal, Quebec, Canada. [2]Division of Surgical Oncology, Department of Surgery, Moores Cancer Centre at UC San Diego Health, La Jolla, California. [3]Department of Medicine, McGill University and the Cancer Program of the Research Institute of the McGill University Health Center, Montreal, Quebec, Canada. [4]Department of Oncology, McGill University and the Cancer Program of the Research Institute of the McGill University Health Center, Montreal, Quebec, Canada.

Note: Supplementary data for this article are available at Molecular Cancer Therapeutics Online (http://mct.aacrjournals.org/).

Current address for M. Hashimoto: Department of Gastroenterological and Transplantation Surgery, Hiroshima University, Kasumi 1-2-3 Minami-ku, Hiroshima, 734-8551, Japan; current address for J.D. Konda: Department of Medical Oncology and Hematology, Princess Margaret Cancer Centre, University Health Network, Toronto, Ontario, Canada; and current address for M. Celia Fernandez: Endocrinology Research Center "Dr. César Bergadá" (CEDIE) CONICET – FEI. Children's Hospital, Buenos Aires, Argentina.

Corresponding Author: Pnina Brodt, The Research Institute of the McGill University Health Centre, Glen Site, 1001 Décarie Boulevard, Room E.02.6220, Montréal, Quebec H4A 3J1, Canada. Phone: 514-934-1934, ext. 36692; Fax: 514-938-7033; E-mail: pnina.brodt@mcgill.ca

Mol Cancer Ther 2021;20:2469–82

doi: 10.1158/1535-7163.MCT-20-0144

resections revealed type I IGF receptor (IGF-IR) overexpression in 53% of the tumors and this correlated with higher tumor grade. Moreover, high IGF-IR expression levels were also observed in the tumor-associated stroma and high IGF-IR expression in both compartments was associated with shorter overall survival and resistance to chemotherapy (22–24).

The major immune cell subtypes of both innate and adaptive immunity including the myeloid-derived mononuclear cells, natural killer (NK) cells and T and B lymphocytes express the IGF-IR and are responsive to IGF ligands (25). Although the role of IGF-IR in the development and function of these cells is complex, there is compelling evidence that within the TME, the IGF axis promotes an anti-inflammatory, immunosuppressive response that enables cancer expansion. IGF-I was shown to negatively regulate dendritic cell (DC) activation, thereby impairing antigen presentation (26) and it was also shown to stimulate the proliferation of immunosuppressive regulatory T cells (Treg; refs. 27–29). IGF-IR activation was also linked to polarization of macrophages to the protumorigenic M2 phenotype (30). IGF targeting was shown to alter the tumor–immune microenvironment (TIME) in colon cancer, reducing anti-inflammatory cytokines (31). IGF-I may also play a role in the tumor-promoting effect of myeloid-derived suppressor cells (MDSC) by regulating TGFβ expression (32). Collectively, these studies identify the IGF axis as a contributor to an anti-inflammatory, protumorigenic TME.

We reported on the bioengineering and characterization of a novel IGF-inhibitor, the IGF-Trap—a fusion protein consisting of the entire extracellular domain of the human IGF-IR fused to the Fc portion of human IgG_1. Similar to the cognate receptor, the IGF-Trap binds the ligands IGF-I and IGF-II (but not insulin) with high affinity, reducing ligand bioavailability in the circulation (ref. 33; and reviewed extensively in ref. 34). We have shown that the IGF-Trap inhibits liver metastases of several highly aggressive carcinomas (33, 35). Moreover, we recently reported that IGF-I could directly induce the expression of N2-associated transcripts *in vitro* in bone marrow–derived neutrophils and moreover, treatment of colon carcinoma MC-38 injected mice with the IGF-Trap, markedly reduced the proportion of immunosuppressive N2-polarized neutrophils infiltrating hepatic metastases (36). These data suggested that inhibition of IGF signaling could reverse the protumorigenic effects of a polarized TME.

Here, we sought to determine whether the IGF-Trap could enhance the efficacy of an immune checkpoint blocker by altering the TIME within hepatic PDAC metastases, thereby potentiating CTL-mediated tumor cell kill to reduce metastatic expansion. We found that IGF axis targeting profoundly altered the immune landscape of hepatic PDAC metastases and enhanced the effect of a PD-1 blocking antibody, causing a marked reduction in metastatic outgrowth.

Materials and Methods

Cells

The pancreatic ductal adenocarcinoma (PDAC) LMP cell line originated from a tumor that arose spontaneously in the genetically engineered Kras G12D/+; p53R172H/+; Pdx1 Cre (KPC) mouse model, and developed in the Lowy laboratory as described in detail elsewhere (37). In syngeneic B6.129 F1 mice implanted in the pancreas with LMP cells, tumor growth and metastasis mimic the aggressive clinical behavior of PDAC. The murine pancreatic cancer line KPC FC1199, referred to here as FC1199, was generated in the Tuveson laboratory (Cold Spring Harbor Laboratory, New York, NY) from PDA tumor tissue obtained from KPC mice of a pure C57BL/6 background, as described previously (38), and was a generous gift from the Tuveson laboratory. Both cell lines were authenticated by the ATCC using Short Tandem Repeat (STR) analysis as described in the National Institute of Standards and Technology (NIST) granted U.S. patent (No. 9,556,482). The cells were routinely tested for common murine pathogens, as per the McGill University Animal Care Committee and the McGill University Biohazard Committee guidelines. *Mycoplasma* testing was carried out routinely using the Applied Biological Materials Mycoplasma PCR Detection Kit (ABM, last relevant test and verification carried out in June 2020, most recently confirmed on August 20, 2021). The cells were routinely grown in a humidified incubator at 37°C with 5% CO_2 in Dulbecco modified Eagle medium (Thermo Fisher Scientific) supplemented with 100 U/mL penicillin and 100 μg/mL streptomycin solution (Sigma), and 10% FBS (Thermo Fisher Scientific). To minimize genetic drifts and phenotype changes, a frozen stock of these cells was maintained and cells thawed and passaged *in vitro* for up to 2–3 weeks only, prior to use in the experiments.

Animals

All mouse experiments were carried out in strict accordance with the guidelines of the Canadian Council on Animal Care (CCAC) "Guide to the Care and Use of Experimental Animals" and under the conditions and procedures approved by the Animal Care Committee of McGill University (AUP number: 5260). Mouse experiments were performed in male and female B6.129 F1 mice that are syngeneic to the LMP cells or in C57Bl/6 male mice that are syngeneic to the FC1199 cells. BL6-Col-GFP mice in which type I collagen is genetically tagged with GFP were a kind gift from Dr. Tatiana Kisseleva (Department of Surgery, University of California, San Diego, La Jolla, CA). They were backcrossed for one generation onto the 129S1/Svlmj (Jackson laboratories) background to obtain heterozygous Col-GFP mice that were crossbred with BL6 mice to generate first generation Bl6.129-Col-GFP F1 mice used for the analysis of activated HSC. All mice were bred in the animal facility of the Research Institute of the McGill University Health Center and used for the experiments at the ages of 7–12 weeks old.

Spontaneous PDAC liver metastasis

Spontaneous PDAC liver metastases were observed following the intra-pancreatic implantation of 5×10^5 LMP cells in 25 μL Matrigel (Corning) mixed with 25 μL PBS, as described (39). Animals were euthanized 21 days post tumor implantation, at which time metastases were visible on the surface of the liver and were enumerated and sized without prior fixation.

Experimental liver metastasis and IGF-Trap treatment

Experimental liver metastases were generated by intrasplenic/portal injections of 1×10^5 or 5×10^5 tumor cells (as indicated), followed by splenectomy as we previously described (40). Animals were euthanized 21 days later, and visible metastases on the surface of the liver were enumerated and sized without prior fixation. Where indicated, fragments of the livers were also fixed in 10% phosphate-buffered formalin, paraffin-embedded, and 5-μm sections stained with hematoxylin and eosin to detect micrometastases and quantify the metastatic burden, as shown. The bioengineering of a third-generation IGF-Trap with improved physicochemical and pharmacodynamic properties was recently described (35). This Trap (IGF-Trap 3.3) was used in all the *in vivo* experiments, as indicated. For immunotherapy the anti PD-1 antibody—Clone RMP1-14 and isotype control rat IgG2a from BioXcell (West Lebanon, NH) were used, as indicated.

NanoString GeoMix digital spatial profiling

The NanoString's GeoMx digital spatial profiling was used to spatially profile formalin-fixed paraffin-embedded (FFPE) sections derived from mice bearing liver metastases. The analysis was performed by the NanoString Pilot Lab. Initially, 12 regions of interest (ROI) (200 μm–600 μm in diameter) were selected within the tumor and IME enriched tissue areas using the following morphology markers: PanCK (Invitrogen/Thermo Fisher clone AE1/AE3), syto83 (Thermo Fisher), CD8 (Abcam, clone EPR21769) and CD45 (Novus, clone EM-05) with additional staining for CD3, αSMA, and F4/80, as required. A cocktail of 46 primary antibodies including IgG isotype controls (rat IgG2a, rat IgG2b, and rabbit IgG) and three housekeeping proteins (Histone H3, Ribosomal protein S6, GAPDH) conjugated to unique oligonucleotide tags with a UV photo-cleavable linker were incubated with 5-μm–thick FFPE sections. The photo-cleaved oligos were then quantified using the optical barcodes in the NanoString's nCounter platform (nCounter Analysis System, NanoString). For analysis, digital counts were first normalized with internal spike-in controls, then with housekeeping genes and the background was subtracted using the IgG controls.

Immunostaining and confocal microscopy

B6129F1 mice were injected via the intrasplenic/portal route with 1×10^5 or 5×10^5 LMP cells as indicated, and the livers perfused at the time intervals indicated, first with PBS and then with 4 mL of a 4% paraformaldehyde solution. The perfused livers were placed in 4% paraformaldehyde for 48 hours and then in 30% sucrose for an additional 48 hours before they were stored at -80°C. For immunostaining, 10-μm cryostat sections were prepared, incubated first in a blocking solution (1% bovine serum albumin (BSA) and 1% FBS in PBS) and then for 1 hour each with the primary antibodies, used at the indicated dilutions, followed by the appropriate Alexa Fluor-conjugated secondary antibodies (the antibodies used in this study are listed in Supplementary Table S1), all at room temperature. Sections stained with the secondary antibodies only were used as controls in all the experiments. After washing with PBS, an autofluorescence quenching kit (VectorTrueVIEW, Burlingame) was used to reduce tissue autofluorescence and sections counterstained with 1 mg/mL 4,6-Diamidino-2-Phenylindole, dihydrochloride (DAPI, Invitrogen). The sections were mounted in the Prolong Gold antifade reagent (Molecular Probes) and confocal images were captured with a Zeiss LSM-880 microscope with a spectrum detection capability. The immunostained cells were quantified blindly in at least 8 images acquired per section, per group.

Isolation of hepatic immune cells and flow cytometry

To analyze early changes in the TIME, mice were injected with 1×10^5 tumor cells via the intrasplenic/portal route and the livers removed 14 days later (or as indicated). Liver homogenates were prepared in cold PBS and filtered through a stainless steel mesh, using a plunger. The filtrates were centrifuged at 500 rpm to separate the hepatocytes, the supernatants containing the non-parenchymal cell fraction centrifuged at 1,400 rpm and the pellets resuspended in 10 mL of a 37.5% Percoll solution in Hank balanced salt solution containing 100 U/mL heparin and centrifuged at 1,910 rpm for 30 minutes to obtain the immune cell–rich fraction. Prior to flow cytometry, red blood cells were removed using the ACK (ammonium chloride-potassium) solution and 1×10^6 cells were immunostained with the indicated antibodies. Data acquisition was with a BD LSRFortessa and FACS Diva software and the data analyzed using the FlowJo software. For FC on hepatic leukocytes, single cells were gated on the basis of size (FSC), granularity (SSC), viability using an eFluor 780 fixable dye (eBioscience, Thermo Fisher) and the expression of CD45.

Ex vivo T-cell activation for analysis of INFγ production

Experimental liver metastases were generated by injecting 1×10^5 LMP cells via the intrasplenic/portal route. Livers were resected 14 days later and immune cell isolated and stimulated for 4 hours with PMA (5 ng/mL; Sigma) and isonomycin (500 ng/mL; Sigma) in the presence of a protein transport inhibitor (BD GolgiStop). The activated T cells were first immunostained for extracellular markers and then fixed and permeabilized for IFNγ staining prior to analysis by FC.

RNA extraction and qPCR

RNA was extracted from G-MDSCs and $CD3^+CD8^+$ T cells using TRIzol (Ambion, Life Technologies). cDNA was synthesized from isolated RNA using a High-Capacity cDNA Reverse Transcription Kit (Applied Biosystems), as per the manufacturer's protocol. qPCR was performed in a Bio-Rad Light Cycler (Bio-Rad), using SYBR (Roche). Two micrograms of total RNA were reverse transcribed and the cDNA analyzed using the primer sets listed in Supplementary Table S1. Changes in expression levels were calculated using the $\Delta\Delta C_t$ values and GAPDH was used to normalize for loading.

T-cell suppression assay

Splenocytes from naïve mice were isolated and red blood cells lysed as described above. Splenic $CD3^+$ T cells were sorted by FACS, stained with CellTrace Carboxyfluorescein succinimidyl ester (CFSE; Thermo Fisher Scientific) and incubated for 48 hours in RPMI with Dynabeads Mouse T-Activator CD3/CD28 (Thermo Fisher Scientific) in a 96-well plate at 37ºC. Liver-derived MDSC from mice which were pretreated, or not, with the IGF-Trap were isolated 14 days post tumor injection and sorted as described above. MDSCs were then added to the preactivated splenic T cells at a ratio of 1:1. In the control condition, no MDSC were added to the activated T cells. After 48 hours of coincubation, the cells were harvested and analysis of CFSE intensity was performed using the BD LSRFortessa.

Data presentation and statistical analyses

The nonparametric Mann–Whitney test was used to analyze all metastasis data and a two-tailed Student *t* test was used to analyze *ex vivo* and *in vitro* data and the IF results. Box-and-whiskers plots were used to show individual values, where applicable. Where indicated, the middle bar denotes the median value, the box limits extend from the 25th to 75th percentiles and the whiskers denote the lowest and highest values. Survival data was analyzed by the Gehan–Breslow–Wilcoxon Test.

Results

The IGF-Trap alters the microenvironment of PDAC liver metastases

We have previously shown that treatment with the IGF-Trap altered the TME in the liver (36, 41) and significantly reduced the outgrowth of liver metastases in several preclinical models of aggressive carcinomas (33, 35). The murine LMP cells originated from the LSL-$Kras^{G12D/+}$;LSL-$Trp53^{R172H/+}$;Pdx-1-Cre (KPC) transgenic model of spontaneous PDAC (42). When implanted orthotopically into the pancreas of syngeneic Bl6.129 F1 mice, these cells mimic the pathology of the human disease and metastasize spontaneously to the liver, eventually causing accumulation of ascites and

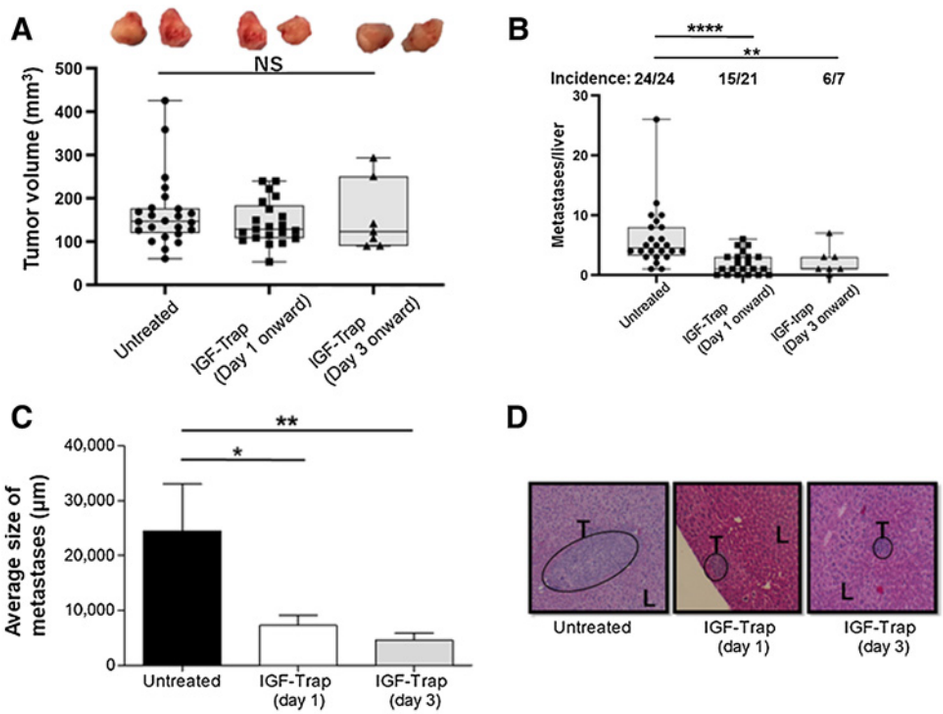

Figure 1.

The IGF-Trap preferentially inhibits the growth of liver metastases in an orthotopic PDAC model. LMP cells (5×10^5 in Matrigel) were implanted in the pancreas of immunocompetent, histocompatible B6/129F1 (B129) male mice. Treatment with 5 mg/kg IGF-Trap 3.3 (or PBS) was initiated 1 [IGF-Trap (Day 1) or 3 (IGF-Trap (Day 3))] days later and continued on alternate days for a total of 5 injections per mouse. Animals were euthanized 3 weeks post tumor implantation, local pancreatic tumors measured and visible metastases on the surface of the liver enumerated. Results are based on pooled data from four independent experiments in which each treatment group consisted of 5–7 mice. Shown in **A** are the volumes of individual local pancreatic tumors of the same mice calculated using the formula 1/2(length $\times$ width^2) with two representative tumors from each of the treatment groups shown on top. Shown in **B** are the numbers of metastases per liver and (on top) the incidence of hepatic metastases per group. Shown in **C** are the average sizes of the metastases expressed as means (±SD) in each group and in **D**, representative H&E-stained PPFE sections of livers from each of the treatment groups. Box and whiskers graphs: the box extends from the 25th to 75th percentiles, the middle line denotes median and the whiskers extends from the minimum to the maximum value. *, $P \leq 0.05$; **, $P < 0.01$; ****, $P < 0.0001$; NS, not significant.

morbidity within 3–4 weeks following implantation (37, 43). We tested the effect of the IGF-Trap on the growth of LMP cells *in vivo* and found that while this treatment had a marked effect on liver metastases, significantly reducing their numbers and sizes (**Fig. 1A–C**), it did not alter local tumor growth in the pancreas (**Fig. 1D**). This suggested that in this model, the IGF-Trap may have exerted its effect on hepatic metastases by altering the TME in the liver. To further investigate this possibility, we profiled the immune microenvironment in the livers of LMP-injected and IGF-Trap treated (or non-treated) mice, using the NanoString GeoMx digital spatial profiler (44), to identify global changes in the expression of immune cell surface markers in the TIME that resulted from IGF-Trap treatment. We analyzed the TIME associated with both micrometastatic lesions and large diffuse liver metastases to distinguish early and late events in immune cell recruitment, and within each liver section, compared the intensity of each signal to that associated with "tumor-free" areas within the same section, to identify changes specific to tumor-infiltrating immune cells (Supplementary Fig. S1A). When relative signal intensities in IGF-Trap and vehicle (PBS)-treated controls were compared, we observed significant differences in the accumulation of several immune cell subtypes in the TME of IGF-Trap treated, as compared to control mice (**Fig. 2A** and **B**). Notable among them were a significant increase in the expression of CD11c and MHCII in both small and large metastases, consistent with increased recruitment and activation of DCs, decreased accumulation of CD11b$^+$ and Ly6G$^+$ cells, consistent with a reduction in bone marrow–derived granulocytic cells (neutrophils or granulocytic (G)-MDSC), increased presence of CD4$^+$ T cells that was accompanied by increased expression of several immune checkpoints [PD-1, T-cell immunoglobulin and mucin domain-containing (TiM)-3 and lymphocyte activation gene (LAG)-3)] in early-stage metastases, and an increase in CD68$^+$ cells accompanied by reduced CD163 expression in the larger metastases, indicative of a reduction in M2 tumor–associated macrophages. In addition, this analysis also revealed a marked reduction in TGFβ1 levels in and around the metastases, consistent with an overall reduction in immunosuppressive signals (**Fig 2B**; Supplementary Fig. S1B).

The IGF-Trap alters the immunosuppressive landscape associated with PDAC liver metastases

Having identified global changes in the liver TIME in IGF-Trap–treated mice, we sought to identify specific immune cell subtypes whose recruitment and/or phenotype were affected by this treatment. We therefore used flow cytometry (FC) and immunofluorescence microscopy (IF) to compare the immune cell infiltrates in mice treated,

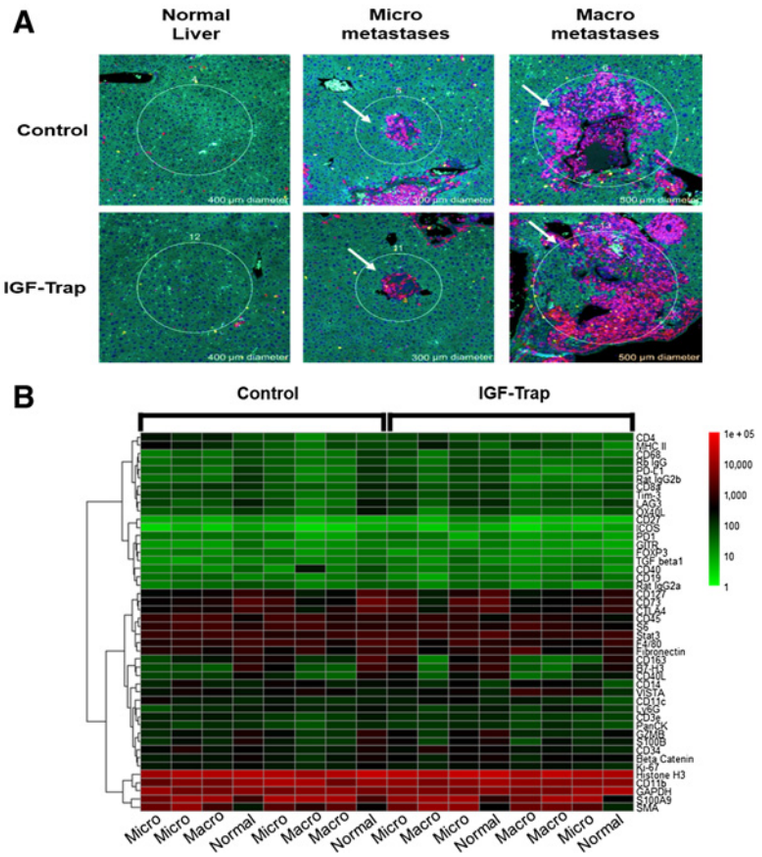

Figure 2.

IGF-Trap treatment alters the tumor immune microenvironment in the liver. Immune-profiling with the NanoString Geomax Profiler was performed on FFPE liver sections that were obtained from mice inoculated via the intrasplenic/portal route with 5×10^5 LMP cells 21 days earlier and treated with a total of five tail vein injections of 5 mg/kg IGF-Trap or PBS (control) on alternate day. Shown in **A** are representative regions of interest (ROI) selected on the basis of the size of the metastases to depict early (micro, $n = 3$) or late (Macro, $n = 3$) immune cell recruitment events. A more detailed image of the ROI selected for analysis can be seen in Supplementary Fig. S1A. Shown in **B** is a heat map generated on the basis of changes in the expression of immune cell surface markers expressed as $\log_{10}$ (fold change) in expression relative to Normal (tumor-free) liver that was used as baseline. Additional information on changes in specific cell surface markers can be seen in Supplementary Fig S1B.

or not, for 2 weeks with the IGF-Trap following the intrasplenic/portal inoculation of LMP cells. We confirmed that IGF-IR activation levels were reduced in $CD11b^+$ myeloid cells by immunohistochemistry (IHC) performed on liver sections from the treated mice (Supplementary Fig. S2). Consistent with the data obtained with the digital profiler, we found that the accumulation of $CD11b^+Ly6C^+Ly6G^+$ myeloid cells, particularly ($CD11b^+Ly6C^{mid}Ly6G^{high}$) G-MDSC was markedly reduced in the livers of IGF-Trap–treated mice, as compared with controls (**Fig. 3A** and see also Supplementary Fig. S3). We also found in the IGF-Trap–treated mice an increased accumulation of ($CD11b^+CD11c^+$) DC that was accompanied by a 35% increase in MHCII expression in these cells (**Fig. 3B**), indicative of their increased activation levels in the treated mice. Consistent with previous findings in a colon carcinoma metastasis model (36), we also found a significant increase in the proportion of Intercellular adhesion molecule (ICAM)-1^+ ($CD11b^+Ly6G^{high}Ly6C^{low}$) neutrophils in the treated mice, indicative of reduced N2 polarization (**Fig. 3C**). Taken together, these results suggested that IGF-Trap-mediated blockade of IGF-IR signaling resulted in an altered and less immunosuppressive TIME in the liver, with an enhanced potential to mount an antitumor immune response. This conclusion was further supported by IHC performed on liver cryostat sections obtained from tumor-bearing mice. Namely, we observed a marked increase in $CD11c^+MHCII^+$ DC around metastatic foci in IGF-Trap–treated mice (**Fig. 3D**, top), as compared with controls. Moreover, in both control and IGF-Trap–treated mice, we detected $F4/80^+CD206^+$ macrophages around the metastases, indicative of the accumulation of M2-polarized TAM in the livers. However, the number of these TAM was significantly reduced (47.3%) in mice treated with the IGF-Trap (**Fig. 3D**, bottom). When G-MDSCs derived from IGF-Trap treated mice were incubated with $CD3^+$ T cells, we found that suppression of T cell proliferation by the MDSC was reduced in comparison to control MDSCs (supplementary Fig. S4), although the difference did not reach statistical significance ($P = 0.08$), likely due to inter-sample variability. Finally, when $CD11b^+LY6G^{high}$ cells were isolated using FACS sorting and their RNA analyzed by qPCR, we found in cells isolated from the IGF-Trap–treated mice a significant reduction in *Vegf* and arginase (*Arg1*) expression (**Fig. 3E**), consistent with reduced immunosuppressive potency.

Taken together, these results identified in IGF-Trap–treated mice a significant shift in the TIME of PDAC liver metastases from a predominantly immunosuppressive and prometastatic TME to one that is more conducive to antitumor immune responses. To determine whether this reduced accumulation and functional potency of immunosuppressive cells was, in fact, associated with increased accumulation in the liver of $CD4^+$ and $CD8^+$ T cells, we performed an IHC analysis on cryostat sections derived from tumor-inoculated mice and found increased accumulation of these T cells in the IGF-Trap–treated mice (**Fig. 4A**).

To determine whether IGF-Trap treatment affected T cell activation and cytokine production in the liver, we isolated immune cells from the livers of LMP-inoculated mice and measured IFNγ production levels following stimulation of the cells with phorbol-12- myristate-13-acetate (PMA) and ionomycin. Flow cytometric analyses revealed increased IFNγ levels in $CD3^+$ $CD8^+$ T cells derived from the IGF-Trap–treated mice (**Fig. 4B**), suggesting an increased functional

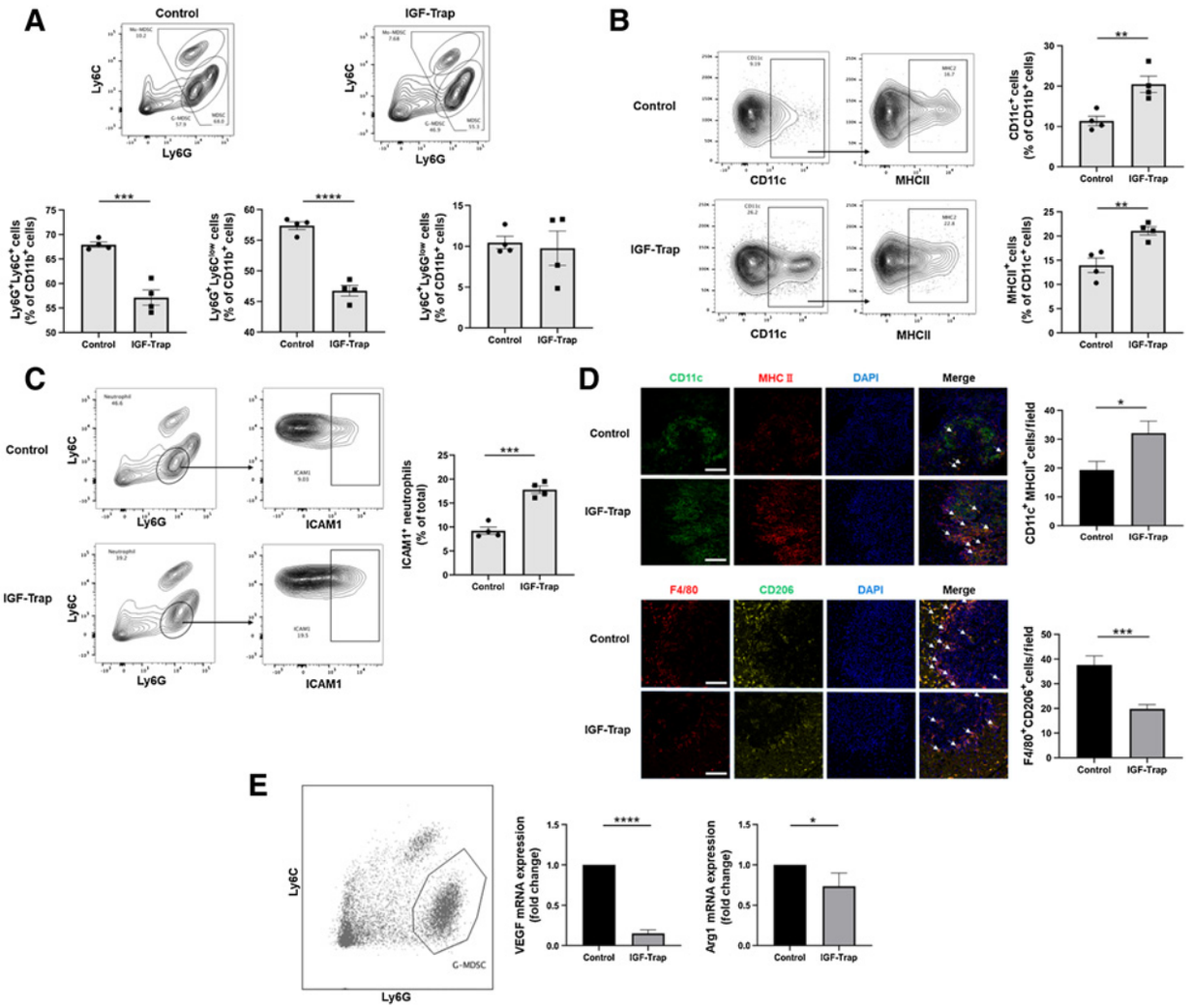

Figure 3.

The IGF-Trap reduces the accumulation of immunosuppressive cells in PDAC liver metastases. Liver immune cells were isolated 14 days post intrasplenic/portal injection of 1×10^5 LMP cells and five intravenous injections of 5 mg/kg IGF-Trap or PBS on alternate days, and immunostained with the indicated antibodies. Shown in (**A**, top) are representative flow cytometric contour plots obtained with each of the indicated immune cell populations that were first gated for size, viability, and CD45 expression (for detailed gating strategy, see Supplementary Fig. S3). Shown in the bar graphs (**A**, bottom) are mean proportions (±SEM) of MDSC, G-MDSC, and Mo-MDSC per liver based on 4 mice per group, analyzed individually. Shown in (**B**, left) are representative flow cytometric contour plots of activated dendritic cells identified based on expression CD11c and MHCII and in the bar graphs (**B**, right) the mean proportions (±SEM) of $CD11b^+MHCII^+$ per liver based on 4 mice per group, analyzed individually. Shown in (**C**, left) are representative contour plots obtained for $CD11b^+Ly6G^{high}Ly6C^{low}$ cells expressing ICAM-1 and in the bar graph (**C**, right) the mean proportions (±SEM) of $Ly6G^+ICAM\text{-}1^+$ cells (markers of N1 neutrophils) in each group based on analysis of four mice. In a separate experiment, the same treatment protocol was used, and cryostat sections prepared for analysis by IHC. Shown in (**D**, left top) are representative confocal images of 10-μm cryostat liver sections immunostained with the indicated antibodies followed by Alexa Fluor 568 (green) for CD11c, Alexa Fluor 647 for MHCII (red), and DAPI (blue). Shown on the right of the confocal images are the mean numbers (±SEM) of the indicated cells per field counted in 15–20 fields per section ($n = 2$ or 3) derived from 3 mice per group. Shown in (**D,** left-bottom) are representative confocal images obtained with the indicated antibodies followed by Alexa Fluor 568 (red) for F4/80, Alexa Fluor 647 (yellow) for CD206, and DAPI (blue). Shown on the right of the confocal images are the means (± SEM) of the indicated cells counted as in (**D**, top). Shown in **E** are results of qPCR analysis performed on RNA extracted from FAC-sorted neutrophils (left). Results in the bar graph are based on three separate analyses and expressed as means (± SD) expression levels (normalized to GAPDH) relative to untreated mice that were assigned a value of 1. Scale bar (**D**), 100 μm. *, $P \le 0.05$; **, $P < 0.01$; ***, $P < 0.001$; ****, $P < 0.0001$.

cytotoxic activity. This was also confirmed when granzyme (Grz)B expression levels were measured by qPCR in $CD3^+CD8^+$ T cells isolated by FACS from similarly treated mice, revealing increased *GrzB* expression levels in T cells isolated from IGF-Trap–treated mice (**Fig. 4C**). Finally, this decrease in the accumulation and function of immunosuppressive cells, coupled with increased T cell activation was associated with a reduction in $Ki67^+$ tumor cells within metastatic foci, suggesting that the number of proliferating tumor cells was markedly reduced (**Fig. 4D**). Collectively, these data strongly suggested that IGF-Trap treatment caused a profound change in the otherwise, immune-tolerant and prometastatic microenvironment associated with metastatic expansion in the liver (45, 46).

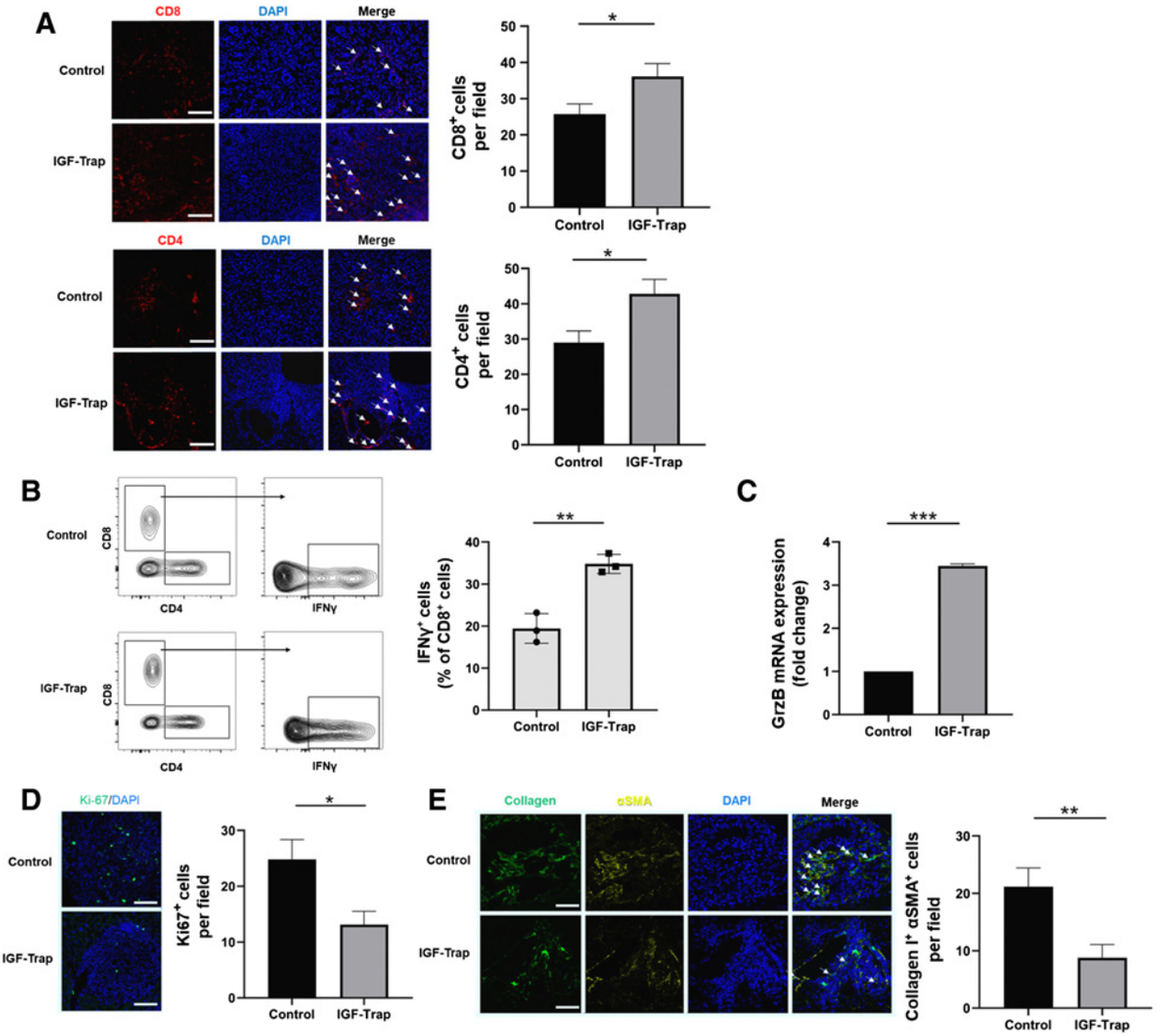

Figure 4.

IGF-Trap treatment enhances T-cell recruitment and potentiates their function in the TME. B6129 F1 mice were injected via the intrasplenic/portal route with 1×10^5 LMP cells, treated with 5 mg/kg IGF-Trap or PBS 1, 4, 7, and 10 days post tumor inoculation and sacrificed on day 14. Shown in **A** are representative confocal images of 10 μm cryostat liver sections immunostained with the indicated antibodies and Alexa Fluor 568 (red) for CD8 (**A**, top), Alexa Fluor 568 (red) for CD4 (**A**, bottom) and DAPI (blue). Shown in the bar graphs (right) are the mean numbers (± SEM) of the indicated cells per field counted in 15–20 fields per section derived from 3 mice per group. Shown in (**B**, left) are results of flow cytometry performed on immune cells which were isolated from mice treated as described in **A** and stimulated for 4 hours with PMA and ionomycin in the presence of a protein transport inhibitor. Shown in the bar graph (**B**, right) are the mean proportions of $CD8^+IFN\gamma^+$ cells per liver (±SEM) based on three livers per group analyzed individually. Shown in **C** are results of qPCR (±SEM) performed on RNA extracted from $CD3^+CD8^+$ T cells that were FACS sorted from livers of tumor-injected mice treated as in **A** (data normalized to GAPDH; $n = 3$), in (**D**, left) representative confocal images of cells immunostained with antibodies to Ki-67 (green) and with DAPI (blue) and in (**D**, right) the mean numbers (±SEM) of $Ki67^+$ cells per field based on 15–20 sections obtained from 3 animals per group. The effect of IGF-Trap on HSC activation (**E**) was analyzed in B6129-Col-GFP mice. Mice were injected via the intrasplenic/portal route with 1×10^5 LMP cells, treated with 5 mg/kg IGF-Trap or PBS on days 2 and 4 post tumor inoculation and sacrificed on day 7. Activated HSC recruited into tumor-infiltrated areas and identified based on type I collagen production and α-SMA expression were quantified. Shown in (**E**, left) are representative confocal images of 10-μm cryostat liver sections immunostained with antibodies to α-SMA followed by Alexa Fluor 568 secondary antibody (yellow), DAPI- stained (blue) and expressing Col-GFP (green). Shown in the bar graph (**E**, right) are the mean numbers of activated HSCs per field (±SEM) based on 15–20 sections obtained from 3 animals per group. Scale bars (**A**, **D**), 100 μm; **E**, 50 μm. *, $P \le 0.05$; **, $P < 0.01$; ***, $P < 0.001$.

Treatment with the IGF-Trap impairs HSC activation

HSCs are activated during the early stages of liver metastasis and play a key role in the induction of a prometastatic microenvironment in this organ (45–47). Normally quiescent within the space of Disse, they are activated in response to factors released by innate immune cells that are recruited to sites of tumor invasion, differentiate into myofibroblast-like cells and characteristically express the myofibroblastic cell surface markers α-smooth muscle actin (α-SMA) and desmin and produce type I collagen (48, 49), as well as immunoregulatory chemokines (48). Previously, we have shown that IGF-I plays a

role in HSC activation in the proinflammatory microenvironment induced by tumor cell entry into the liver (41). To investigate the effect of the IGF-Trap on HSC activation following injection of LMP cells, we used the Bl6.129-Col-GFP mice, in which type I collagen (ColI) is genetically GFP-tagged and activated HSC can be identified on the basis of coexpression of GFP-ColI and α-SMA. Consistent with our previous findings (41), we found here that treatment of these mice with the IGF-Trap significantly reduced HSC activation in response to the metastatic cells (**Fig. 4E**).

The IGF-Trap inhibits the growth of experimental PDAC liver metastases

Having observed the marked differences in the immunosuppressive landscape within the TIME of liver metastases in mice treated with the IGF-Trap, we next analyzed how these changes affected metastatic expansion following injection of LMP cells via the intrasplenic/portal route to generate experimental liver metastases. Because we have previously observed a sexual dimorphism in the control of the TIME of liver metastases (as reported in ref. 43), we performed the experiments in age-matched male and female mice to rule out sex-specific effects. In both sexes, we observed a significant reduction in the numbers and sizes of liver metastases (**Fig. 5A–H**), as compared with vehicle-treated controls, when using the protocol depicted in **Fig. 5I**. This suggested that the changes in the TIME impacted metastatic expansion in the livers of the treated mice, regardless of their sex.

The IGF-Trap and immunotherapy reciprocally enhance their inhibitory effects on liver metastasis

The failure of PDAC patients to respond to immunotherapy is thought to be due, at least in part, to immunosuppressive cells such as

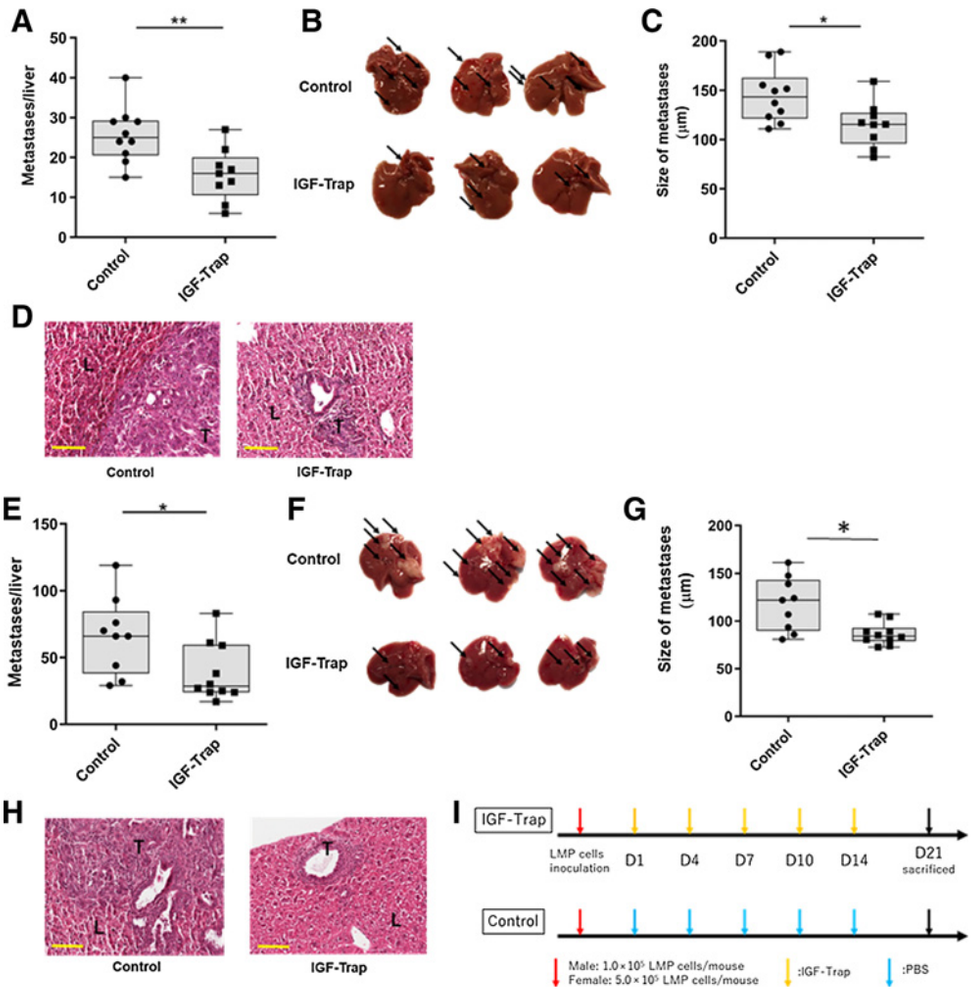

Figure 5.

The IGF-Trap inhibits the growth of pancreatic carcinoma liver metastases. Experimental liver metastases were generated by inoculation of 1×10^5 (for males, **A–D**) or 5×10^5 (for females, **E–H**) LMP cells via the intrasplenic/portal route. The number of mice injected was 10 (vehicle) and 9 (IGF-Trap) male mice and 9 (vehicle) and 10 (IGF-Trap) female mice. Treatment with 5 mg/kg IGF-Trap was initiated 1 day later and continued twice weekly for a total of 5 injections per mouse (**I**). Mice were sacrificed 21 days post tumor inoculation and visible metastases on the surface of the liver enumerated prior to fixation. Results are based on two experiments each for male and female mice. Shown in (**A** and **E**) are the numbers of metastases per each liver. Shown in (**B** and **F**) are representative livers from each group where arrows denote visible metastases. Shown in (**C** and **G**) are the mean diameters of metastases per liver and in (**D** and **H**) representative images of H&E-stained FFPE liver sections ($n = 9$). Scale bar, 100 μm. Box and whiskers graphs: the box extends from the 25th to 75th percentiles, the middle line denotes median and the whiskers extend from the minimum to the maximum values. T, tumor; L, liver; *, $P < 0.05$; **, $P < 0.01$.

polarized TAMs and MDSCs that infiltrate the primary tumors (16, 18). While the TIME associated with PDAC liver metastases has not been extensively explored (partially because surgical resections of PDAC liver metastases are rare), we have recently documented the accumulation of immunosuppressive cells such as G-MDSCs and monocytic (Mo)-MDSC in the livers of mice bearing spontaneous or experimental LMP metastases (43). The data above have clearly shown that IGF-Trap treatment caused a reduction in the accumulation and/or polarization of several immunosuppressive cell types in the livers. Of significance, however, the increased accumulation of T cells in the treated mice was also associated with increased expression of PD-1 (**Fig. 2B**; Supplementary Fig. S1). We also confirmed the expression of PD ligand (PD-L)1 in LMP cells, as well as in a second PDAC cell line the FC1199 cells syngeneic to C57Bl/6 mice (Supplementary Fig. S5). We asked therefore whether combining a PD-1 inhibitor with the IGF-Trap will have a reciprocal enhancing effect, potentiating antitumor immunity in this organ, and further reducing the metastatic burden. Mice inoculated with LMP cells via the intrasplenic/portal route were treated on alternate days with 5 mg/kg IGF-Trap or 10 mg/kg of an anti-murine PD-1 antibody (or a nonimmune IgG isotype as control) for a total of 5 injections each over a period of 15 days (see time line in Supplementary Fig. S6). Liver metastases were then enumerated 21 days post tumor injection and compared with mice injected with each of these inhibitors alone. As expected, treatment with the IGF-Trap reduced liver metastasis when used alone and the addition of the IgG isotype control to the IGF-Trap had no effect on the metastatic burden. Treatment with the anti–PD-1 antibody alone also reduced the number of liver metastases, suggesting that blockade of this immune checkpoint enabled an antitumor immune response in these mice. These tumor-inhibitory effects were enhanced, when the two treatments were combined and this was observed in both male (**Fig. 6A–E**) and female (**Fig. 6F–J**) mice, and reflected in further reductions in both the median number and mean size of the metastases, revealing an additive inhibitory effect on the growth of liver metastases when the two drugs were combined. This marked effect of the combinatorial immunotherapy on liver metastases was not specific to the strain or the LMP model, as similar effects were also observed when C57Bl/6 mice were injected with the syngeneic FC1199 cells and treated in a similar manner (Supplementary Fig. S7). Furthermore, mice that were continuously treated with the combinatorial immunotherapy had a significantly prolonged survival, as compared with untreated mice, whereas treatment with the IGF-Trap or anti–PD-1 antibodies alone had a more minor (and not statistically significant) effect on survival (**Fig. 6K**).

To elucidate the mechanism of action of the combinatorial treatment, we compared the immune cell infiltrate in mice injected with LMP cells treated with each of the inhibitors alone or with the combination, using FC and IF. Tumor-injected mice were treated as indicated (**Fig. 7**) and their livers analyzed 14 days post tumor inoculation. As expected, we observed a significant decrease in MDSC accumulation in IGF-Trap–treated mice, as well as in mice that received the combination therapy, as compared to control mice or mice treated with the anti–PD-1 antibody, and this was particularly evident for the accumulation $Ly6G^{high}$ G-MDSCs (**Fig. 7A**). In mice treated with anti-PD-1 antibodies (alone or in combination with IGF-Trap), we observed a significant increase in the accumulation of both $CD4^+$ and $CD8^+$ T cells and a corresponding decrease in PD-1 expression on $CD8^+$ cells, and this was confirmed by both FC and IF. However, no change was observed in the expression of CTLA-4 or LAG3 on these cells (**Fig. 7B–D**). Finally, FC revealed a marked increase in IFNγ-producing $CD8^+$ T cells in mice treated with the combinatorial therapy as compared to single agent–treated mice (**Fig. 7E**) and in addition, *GrzB* mRNA levels in T cells isolated from mice treated with IGF-Trap and combinatorial therapy were also significantly increased relative to controls (**Fig. 7F**). Together, these data showed a potentiation of a T-cell response that was optimal in mice treated with the combination therapy.

Discussion

Despite recent successes of single-agent immunotherapy in the treatment of several highly aggressive malignancies, the majority of cancers, including PDAC remain unresponsive. This, despite evidence of T cell–activating tumor antigens on PDAC cells (reviewed in refs. 50, 51). Among several factors that may contribute to this failure to respond are the production of immunosuppressive IL10 and TGFβ by PDAC cells and the recruitment to the tumor site of immunosuppressive cells such as MDSC and M2 TAM (ref. 52; reviewed in ref. 19). This may be particularly true in the liver, where recruitment of immunosuppressive bone marrow–derived myeloid cells (BMDC) was documented prior to (53, 54), and following tumor cell entry into the liver (45, 46). Thus, combination therapies that can activate cytotoxic T cells, while also targeting immunosuppressive cells in the TME hold much promise in the treatment of this disease. In this study, we show for the first time, that targeting the IGF axis alters the TIME of PDAC liver metastases, reducing the recruitment and activity of several immunosuppressive cell types and resulting in increased T-cell accumulation in the liver. Treatment with anti–PD-1 antibodies, on the other hand, while not directly increasing T-cell recruitment, decreased the proportion of $PD\text{-}1^+$ T cells. Our results suggest that the combined effect of increased T-cell numbers (caused mainly by IGF-Trap treatment) and decreased T-cell exhaustion (due to anti PD-1 antibody) was an enhancement of T cell activity, and this resulted in the more potent antimetastatic effect of the combinatorial therapy (see diagram in **Fig. 8**).

Intriguingly, although the growth of liver metastases in animals treated with the IGF-Trap was inhibited, we did not observe a difference in the growth of the local, orthotopically implanted pancreatic tumors in the same mice. We have previously documented differences in the TME of local pancreatic LMP tumors and their hepatic metastases. While a high proportion of MDSC identified in the liver were of the Mo-MDSC subset, this population was lacking in the pancreatic tumors (43). Mo-MDSC were among immune cell types affected by IGF-Trap treatment and their absence in the pancreatic tumors may be one factor affecting the differential response to the treatment. In addition, we observed that the liver is the main site of IGF-Trap accumulation (35), and a lower bioavailability in the pancreatic tumors may have contributed to the divergent effect.

We have shown here that IGF-Trap treatment profoundly altered the immune landscape of liver metastases, affecting a multiplicity of immune cell types. IGF-IR is widely expressed on innate and adaptive immune cells (55, 56), and IGF-IR blockade could, therefore, affect the recruitment and/or function of each of these cell types directly. Alternatively (or in addition to), this broad effect may be due to transcriptional regulation of a central factor regulating immunosuppression in the liver. We have previously shown that treatment of bone marrow-derived $CD11b^+Ly6G^+$ cells with IGF-I upregulated the expression of both TGFβ1 and VEGF (36), and as we have shown here (**Fig. 2**; Supplementary Fig. S1), IGF-Trap treatment significantly reduced TGFβ1 levels in the TME of liver metastases, at both early and late stages of expansion. This could account for the overall reduction in the accumulation of tumor-associated immunosuppressive cells such

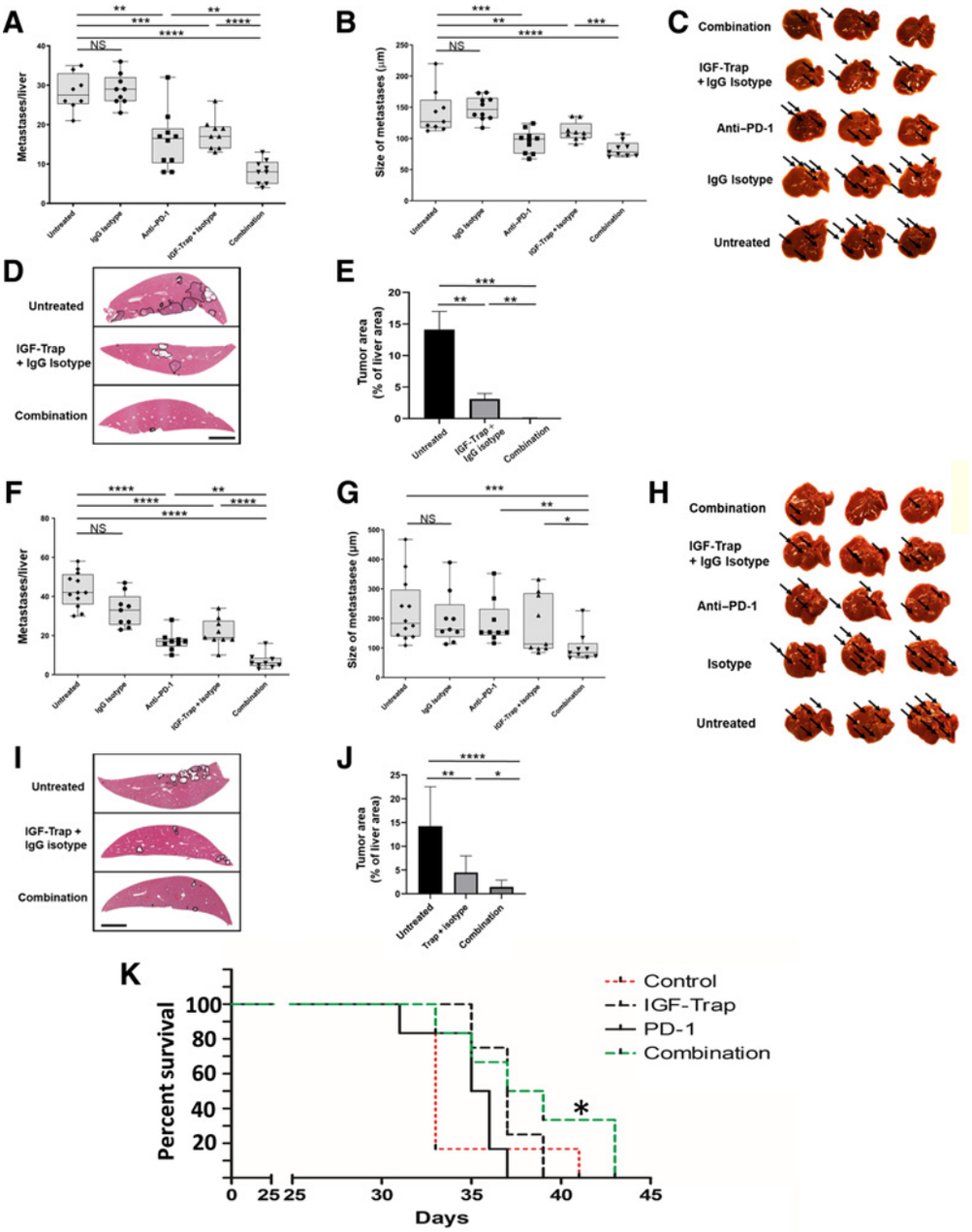

Figure 6.

Combinatorial IGF-Trap/anti–PD-1 therapy further decreases the number of liver metastases and prolongs survival. Experimental liver metastases were generated by the inoculation of 1×10^5 (for males, **A–E**), and 5×10^5 (for females, **F–J**) LMP cells via the intrasplenic/portal route. Treatment with 5 mg/kg IGF-Trap (or PBS) i.v. was initiated 1 day post tumor inoculation and continued twice weekly for a total of 5 injections per mouse. Treatment with 10 mg/kg anti-PD-1 or the IgG isotype control was administered i.p. on alternate days for a total of 5 injections per mouse (see Supplementary Fig. S6). A total of 9–10 male mice and 9–12 female mice were injected per treatment group. Mice were sacrificed on day 21 and visible liver metastases enumerated without prior fixation. Results are based on two experiments each, for male and female mice. Shown in (**A** and **F**) are the numbers of metastases counted per liver and in (**B** and **G**) the mean diameters of the visible metastases per liver. There were no significant differences in either the numbers or sizes of metastases between untreated mice and mice treated with the IgG isotype control. Shown in (**C** and **H**) are representative livers from each group where arrows denote metastases. Shown in (**D** and **I**) are representative images of H&E-stained FFPE liver sections where metastases are encircled and in (**E** and **J**) the means of total tumor surface area per section (±SEM) expressed as % of total liver surface area and based on analysis of nine sections per group (Scale bar, 100 μm). *, $P \le 0.05$; **, $P < 0.01$; ***, $P < 0.001$; ****, $P < 0.0001$; NS, not significant. To test the effect of the combinatorial therapy on survival, syngeneic B6.129 F1 female mice were injected via the intrasplenic/portal route with 1×10^5 LMP tumor cells (5 mice per group) and treatment with 5 mg/kg IGF-Trap (or vehicle) i.v. was initiated 1 day post tumor inoculation and continued twice weekly. Treatment with 10 mg/kg anti–PD-1 antibody i.p. was administered on alternate days. The treatments continued for a total of 5 weeks or until animals were moribund and euthanized. Shown in **K** is a Kaplan–Meier plot for each of the treatment groups. *, $P < 0.05$ as assessed by the Gehan–Breslow–Wilcoxon Test.

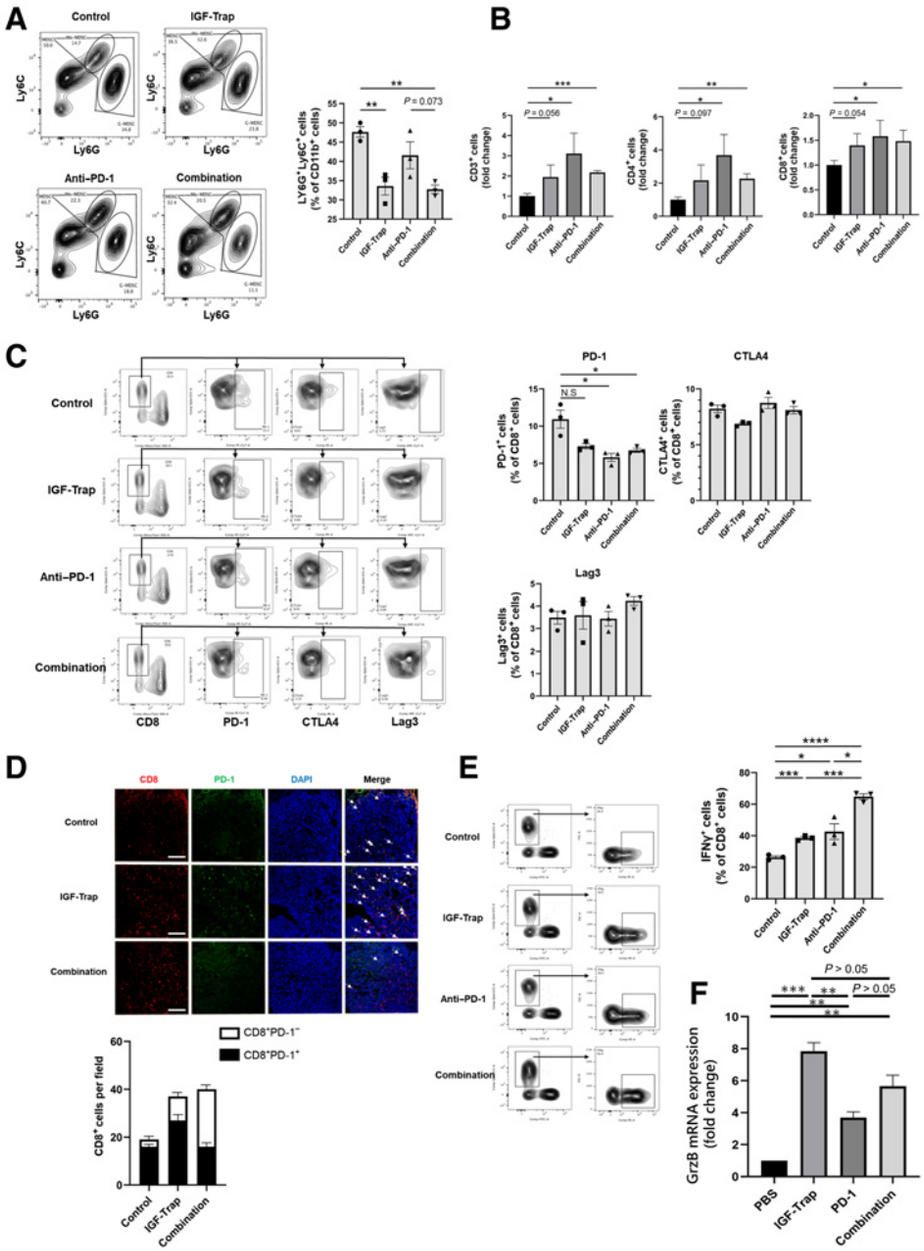

Figure 7.

Increased T-cell recruitment and decreased PD-1 expression in the liver TME following combinatorial therapy. Liver immune cells were isolated 14 days post intrasplenic/portal injection of 1×10^5 LMP cells and the treatment protocol described in the legend to **Fig 6** and analyzed by flow cytometry. Shown in (**A**, left) are representative flow cytometric contour plots obtained with each of the indicated immune cells populations that were first gated as outlined in Supplementary Fig. S3, and in the bar graphs (**A**, right) the mean proportions (%; ±SEM) of MDSC per liver based on 3 mice per group, analyzed individually. Shown in **B** are the mean numbers of the indicated cells obtained per liver (±SEM) expressed as a ratio to untreated mice that were assigned a value of 1 and based on 3 mice per group, analyzed individually. Shown in **C** are representative contour plots obtained for $CD8^+$ cells immunostained with antibodies to the indicated immune checkpoints and in the bar graphs the relative proportions (%) of positive T cells (±SEM) based on the analyses of 3 livers per group. Shown in (**D,** top) are representative confocal images of 10-μm cryostat liver sections immunostained with the indicated antibodies followed by Alexa Fluor 568 (red) for CD8, Alexa Fluor 647 for PD-1 (green), and DAPI (blue) and in (**D,** bottom) are the mean numbers (±SEM) of the $CD8^+$ T cells per field (expressing or not PD-1), counted in 15–20 fields per section derived from 3 mice per group. Note that the number of $CD8^+$ T cells increased significantly in both IGF-Trap and combination therapy-treated mice but the ratio of PD-1^+:$CD8^+$ cell decreased significantly only in mice that received the combination therapy. Shown in (**E**, left) are results of flow cytometry performed on immune cells which were isolated from mice treated as in **A** and stimulated for 4 hours as described in the legend to **Fig 4**. Shown in the bar graph (**E,** right) are the mean proportions of $CD8^+IFN\gamma^+$ cells per liver (±SEM) based on 3 livers per group, analyzed individually. Scale bar, 100 μm; Shown in **F** are results of qPCR (±SEM) performed on RNA extracted from $CD3^+CD8^+$ T cells that were FAC sorted from livers of tumor-injected mice treated as in **A** (data normalized to GAPDH; $n = 3$). *, $P \le 0.05$; **, $P < 0.01$; ***, $P < 0.001$; ****, $P < 0.0001$; NS, not significant.

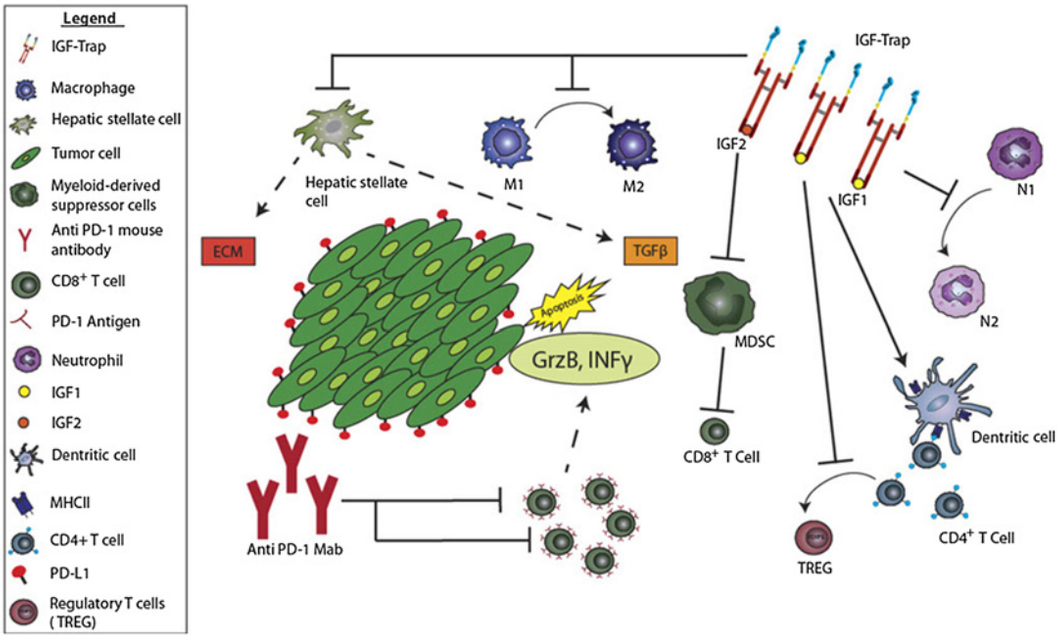

Figure 8.

The combined effect of the IGF-Trap and anti–PD-1 antibodies on the tumor microenvironment in the liver. Shown is a diagrammatic representation of the proposed effects of the combinatorial immunotherapy on the TME of PDAC liver metastases. The IGF-Trap reduces TAM and neutrophil polarization, MDSC accumulation, and HSC activation, while also enhancing DC activation and enabling antigen presentation. This results in increased accumulation of $CD8^+$ T cells in the TME. Anti–PD-1 antibodies reduce T-cell exhaustion and this is associated with potentiation of $CD8^+$ T-cell activity as reflected in increased IFNγ and GrzB production and results in increased tumor cell death.

as MDSC, M2 macrophages, and N2 neutrophils that are commonly regulated by TGFβ (46). Furthermore, because the recruitment of neutrophils and monocytes are early events in the mobilization of innate immune cells into the ME of liver metastases, triggering later events such as activation of HSC that are an additional source of TGFβ (45), a blockade of IGF-IR signaling in these cells could result in a general decrease in the recruitment of immunosuppressive cells and thereby, increased accumulation and activation of T cells. Using a tumor-free model, we have also previously shown that reduced IGF-I bioavailability impairs hepatic stellate cell activation directly (41). Thus, direct and indirect effects on HSC could contribute to a state of enhanced antitumor immunity. We have previously reported that although the IGF-Trap consists of the extracellular domain of the human receptor, no humoral response to this protein could be detected in injected mice (33). However, we cannot entirely rule out the possibility that an immune response to the IGF-Trap played some role or that a direct effect on tumor cell proliferation in the liver also contributed.

Our results add to the growing body of evidence that immunotherapy can be rendered more effective when combined with strategies that target the TME in PDAC and other advanced solid and treatment-refractory tumors. Some combinations with targeted therapy (e.g., ref. 57 and www.clinicaltrials.org - NCT02758587) and chemotherapy (NCT03977272, NCT03983057) have, in fact, already advanced to clinical trials (reviewed in ref. 19). Diana and colleagues, analyzing the prognostic value of PD-1/PD-L1 expression together with infiltration of $CD8^+$ lymphocytes and Treg in 145 surgical PDAC resections found that both $PD\text{-}1^+$ and $CD8^+$ T-cell infiltrates were independent prognostic markers in patients treated with adjuvant chemotherapy, predicting a better outcome (58). Moreover, a genomic analysis recently identified a PDAC subtype with increased activation of $CD8^+$ T cells and overexpression of CTLA-4 and PD-1 within surgical resections that corresponded to higher frequency of somatic mutations and tumor-specific neoantigens (59), suggesting that patient stratification based on mutational signatures may identify a patient subpopulation particularly sensitive to immunotherapy. Collectively, these data identify PDAC as a malignancy that may be highly responsive to immune-based therapy under optimizing conditions. In our model, we found a significant effect on liver metastases when mice were treated with a single checkpoint inhibitor, namely anti–PD-1 antibodies, despite an unaltered expression of both CTLA-4 and LAG3 on $CD8^+$ T cells. This suggests that the effect of immunotherapy, in this model, may be even further optimized by combining several immune checkpoint blockers with IGF-Trap treatment, and this may also be required in the clinical management of this disease.

Liver metastases were identified as one of several factors predictive of poor response to immunotherapy (60, 61). This could be a contributing factor to the resistance of PDAC to immunotherapy, as a large proportion of patients with PDAC already harbor hepatic metastases at the time of diagnosis or relapse with liver metastases following surgical excision of the primary tumor. Our data, taken together with other findings, suggest that for patients with resectable primary PDAC tumors that are free of liver metastases at the time of diagnosis, combining immunotherapy with targeted anti-IGF-IR therapy could improve treatment outcome.

Authors' Disclosures

A.M. Lowy reports personal fees from Tanabe, Corcept, Autobahn, and personal fees from Kinnate outside the submitted work. P. Brodt reports grants from MITACS, McGill University Health Center Foundation, and grants from Canadian Institute for

Health Research during the conduct of the study; in addition, P. Brodt has a patent for Soluble IGFR Fc Fusion Proteins and Uses Thereof Application No. 12857915.8 Case Ref. 05001770-467EP European Patent Office issued, a patent for Novel Soluble IGF Receptor Fc Fusion Proteins For The Treatment Of Cancer And Metastasis - US - International (PCT) Patent Application No. PCT/CA2012/050899 United States issued, and a patent for Therapeutic Applications Of Type 1 Insulin-Like (IGF-1) Receptor Antagonists - United States Provisional Patent Application No. 63/120,442. pending. No disclosures were reported by the other authors.

Authors' Contributions

M. Hashimoto: Data curation, formal analysis, investigation, methodology, writing–original draft. **J.D. Konda:** Data curation, methodology. **S. Perrino:** Data curation, methodology. **M.C. Fernandez:** Data curation, methodology. **A.M. Lowy:** Resources, writing–review and editing. **P. Brodt:** Conceptualization, resources, formal analysis, supervision, funding acquisition, investigation, writing–original draft, writing–review and editing.

Acknowledgments

The authors acknowledge with gratitude the staff of the Immunophenotyping Facility of the Research Institute of the McGill University Health Center and in particular, Marie-Helene Lacombe and Ekaterina Iourtchenko, for their help with flow cytometry and cell sorting, Simon Milette for his assistance with flow cytometry analyses, the NanoString Technologies scientific staff, in particular Drs. Liang Zhang and Yan Liang, for excellent support in the analysis of the GeoMax immune profiling data and Dr. Matthew Leibovitch (Research Institute of the Mcgill University Health Center) for his help with data analysis. Dr. Masakazu Hashimoto was the recipient of the Oversea Medical Research Grant from Sumitomo Life welfare and Culture Foundation, a Research Fellowship from the Uehara memorial Foundation and a fellowship from the Research Institute of the McGill University Health Center. This work was made possible by grant PP2-141724 from the Canadian Institute for Health Research, and grant IT04483 from MITACS (to P. Brodt). Research support from the MUHC Foundation and the MI4 initiative of McGill University (to P. Brodt) and NIH award CA155620 (to A.M. Lowy) are also gratefully acknowledged.

The costs of publication of this article were defrayed in part by the payment of page charges. This article must therefore be hereby marked *advertisement* in accordance with 18 U.S.C. Section 1734 solely to indicate this fact.

Received February 24, 2020; revised May 13, 2021; accepted September 15, 2021; published first September 22, 2021.

References

1. Ferlay J, Shin HR, Bray F, Forman D, Mathers C, Parkin DM. Estimates of worldwide burden of cancer in 2008: GLOBOCAN 2008. Int J Cancer 2010;127:2893–917.
2. Siegel RL, Miller KD, Jemal A. Cancer statistics, 2015. CA Cancer J Clin 2015;65:5–29.
3. Siegel RL, Miller KD, Jemal A. Cancer statistics, 2018. CA Cancer J Clin 2018;68:7–30.
4. Rahib L, Smith BD, Aizenberg R, Rosenzweig AB, Fleshman JM, Matrisian LM. Projecting cancer incidence and deaths to 2030: the unexpected burden of thyroid, liver, and pancreas cancers in the United States. Cancer Res 2014;74:2913–21.
5. Tempero MA, Malafa MP, Behrman SW, Benson AB 3rd, Casper ES, Chiorean EG, et al. Pancreatic adenocarcinoma, version 2.2014: featured updates to the NCCN guidelines. J Natl Compr Canc Netw 2014;12:1083–93.
6. Torre LA, Siegel RL, Ward EM, Jemal A. Global cancer incidence and mortality rates and trends–an update. Cancer Epidemiol Biomarkers Prev 2016;25:16–27.
7. David M, Lepage C, Jouve JL, Jooste V, Chauvenet M, Faivre J, et al. Management and prognosis of pancreatic cancer over a 30-year period. Br J Cancer 2009;101:215–8.
8. Hess KR, Varadhachary GR, Taylor SH, Wei W, Raber MN, Lenzi R, et al. Metastatic patterns in adenocarcinoma. Cancer 2006;106:1624–33.
9. Inoue K, Hiraoka T, Kanemitsu K, Takamori H, Tsuji T, Kawasuji M. Onset of liver metastasis after histologically curative resection of pancreatic cancer. Surg Today 2006;36:252–6.
10. Seufferlein T, Bachet JB, Van Cutsem E, Rougier P, Group EGW. Pancreatic adenocarcinoma: ESMO-ESDO Clinical Practice Guidelines for diagnosis, treatment and follow-up. Ann Oncol 2012;23:vii33–40.
11. Khushman M, Dempsey N, Maldonado JC, Loaiza-Bonilla A, Velez M, Carcas L, et al. Full dose neoadjuvant FOLFIRINOX is associated with prolonged survival in patients with locally advanced pancreatic adenocarcinoma. Pancreatology 2015;15:667–73.
12. Franklin C, Livingstone E, Roesch A, Schilling B, Schadendorf D. Immunotherapy in melanoma: Recent advances and future directions. Eur J Surg Oncol 2017;43:604–11.
13. Muto A, Gridelli C. New immunotherapy in the treatment of advanced renal cancer. Expert Opin Emerg Drugs 2019:24:233–7.
14. Osmani L, Askin F, Gabrielson E, Li QK. Current WHO guidelines and the critical role of immunohistochemical markers in the subclassification of non-small cell lung carcinoma (NSCLC): Moving from targeted therapy to immunotherapy. Semin Cancer Biol 2018;52:103–9.
15. Nevala-Plagemann C, Hidalgo M, Garrido-Laguna I. From state-of-the-art treatments to novel therapies for advanced-stage pancreatic cancer. Nat Rev Clin Oncol 2020;17:108–23.
16. Upadhrasta S, Zheng L. Strategies in developing immunotherapy for pancreatic cancer: recognizing and correcting multiple immune "Defects" in the tumor microenvironment. J Clin Med 2019;8:1472.
17. Sakellariou-Thompson D, Forget MA, Creasy C, Bernard V, Zhao L, Kim YU, et al. 4–1BB agonist focuses CD8(+) tumor-infiltrating T-cell growth into a distinct repertoire capable of tumor recognition in pancreatic cancer. Clin Cancer Res 2017;23:7263–75.
18. Aroldi F, Zaniboni A. Immunotherapy for pancreatic cancer: present and future. Immunotherapy 2017;9:607–16.
19. Bear AS, Vonderheide RH, O'Hara MH. Challenges and opportunities for pancreatic cancer immunotherapy. Cancer Cell 2020;38:788–802.
20. Bergmann U, Funatomi H, Yokoyama M, Beger HG, Korc M. Insulin-like growth factor I overexpression in human pancreatic cancer: evidence for autocrine and paracrine roles. Cancer Res 1995;55:2007–11.
21. Subramani R, Lopez-Valdez R, Arumugam A, Nandy S, Boopalan T, Lakshmanaswamy R. Targeting insulin-like growth factor 1 receptor inhibits pancreatic cancer growth and metastasis. PLoS One 2014;9:e97016.
22. Thomas D, Radhakrishnan P. Role of tumor and stroma-derived IGF/IGFBPs in pancreatic cancer. Cancers 2020;12:1228.
23. Ireland L, Santos A, Ahmed MS, Rainer C, Nielsen SR, Quaranta V, et al. Chemoresistance in pancreatic cancer is driven by stroma-derived insulin-like growth factors. Cancer Res 2016;76:6851–63.
24. Valsecchi ME, McDonald M, Brody JR, Hyslop T, Freydin B, Yeo CJ, et al. Epidermal growth factor receptor and insulinlike growth factor 1 receptor expression predict poor survival in pancreatic ductal adenocarcinoma. Cancer 2012;118:3484–93.
25. Smith TJ. Insulin-like growth factor-I regulation of immune function: a potential therapeutic target in autoimmune diseases? Pharmacol Rev 2010;62:199–236.
26. Xuan NT, Hoang NH, Nhung VP, Duong NT, Ha NH, Hai NV. Regulation of dendritic cell function by insulin/IGF-1/PI3K/Akt signaling through klotho expression. J Recept Signal Transduct Res 2017;37:297–303.
27. Bilbao D, Luciani L, Johannesson B, Piszczek A, Rosenthal N. Insulin-like growth factor-1 stimulates regulatory T cells and suppresses autoimmune disease. EMBO Mol Med 2014;6:1423–35.
28. Chellappa S, Hugenschmidt H, Hagness M, Line PD, Labori KJ, Wiedswang G, et al. Regulatory T cells that co-express RORgammat and FOXP3 are pro-inflammatory and immunosuppressive and expand in human pancreatic cancer. Oncoimmunology 2016;5:e1102828.
29. Miyagawa I, Nakayamada S, Nakano K, Yamagata K, Sakata K, Yamaoka K, et al. Induction of regulatory T cells and its regulation with insulin-like growth Factor/Insulin-like growth factor binding protein-4 by human mesenchymal stem cells. J Immunol 2017;199:1616–25.
30. Barrett JP, Minogue AM, Falvey A, Lynch MA. Involvement of IGF-1 and Akt in M1/M2 activation state in bone marrow-derived macrophages. Exp Cell Res 2015;335:258–68.
31. Sanchez-Lopez E, Flashner-Abramson E, Shalapour S, Zhong Z, Taniguchi K, Levitzki A, et al. Targeting colorectal cancer via its microenvironment by inhibiting IGF-1 receptor-insulin receptor substrate and STAT3 signaling. Oncogene 2016;35:2634–44.

32. Shaw AK, Pickup MW, Chytil A, Aakre M, Owens P, Moses HL, et al. TGFbeta signaling in myeloid cells regulates mammary carcinoma cell invasion through fibroblast interactions. PLoS One 2015;10:e0117908.
33. Wang N, Rayes RF, Elahi SM, Lu Y, Hancock MA, Massie B, et al. The IGF-trap: novel inhibitor of carcinoma growth and metastasis. Mol Cancer Ther 2015;14: 982–93.
34. Chen YM, Qi S, Perrino S, Hashimoto M, Brodt P. Targeting the IGF-axis for cancer therapy: development and validation of an IGF-trap as a potential drug. Cells 2020;9:1098.
35. Vaniotis G, Moffett S, Sulea T, Wang N, Elahi SM, Lessard E, et al. Enhanced anti-metastatic bioactivity of an IGF-TRAP re-engineered to improve physicochemical properties. Sci Rep 2018;8:17361.
36. Rayes RF, Milette S, Fernandez MC, Ham B, Wang N, Bourdeau F, et al. Loss of neutrophil polarization in colon carcinoma liver metastases of mice with an inducible, liver-specific IGF-I deficiency. Oncotarget 2018;9:15691–704.
37. Tseng WW, Winer D, Kenkel JA, Choi O, Shain AH, Pollack JR, et al. Development of an orthotopic model of invasive pancreatic cancer in an immunocompetent murine host. Clin Cancer Res 2010;16:3684–95.
38. Hingorani SR, Wang L, Multani AS, Combs C, Deramaudt TB, Hruban RH, et al. Trp53R172H and KrasG12D cooperate to promote chromosomal instability and widely metastatic pancreatic ductal adenocarcinoma in mice. Cancer Cell 2005;7: 469–83.
39. Jiang YJ, Lee CL, Wang Q, Zhou ZW, Yang F, Jin C, et al. Establishment of an orthotopic pancreatic cancer mouse model: cells suspended and injected in Matrigel. World J Gastroenterol 2014;20:9476–85.
40. Ham B, Wang N, D'Costa Z, Fernandez MC, Bourdeau F, Auguste P, et al. TNF receptor-2 facilitates an immunosuppressive microenvironment in the liver to promote the colonization and growth of hepatic metastases. Cancer Res 2015;75: 5235–47.
41. Fernandez MC, Rayes R, Ham B, Wang N, Bourdeau F, Milette S, et al. The type I insulin-like growth factor regulates the liver stromal response to metastatic colon carcinoma cells. Oncotarget 2017;8:52281–93.
42. Frese KK, Tuveson DA. Maximizing mouse cancer models. Nat Rev Cancer 2007; 7:645–58.
43. Milette S, Hashimoto M, Perrino S, Qi S, Chen M, Ham B, et al. Sexual dimorphism and the role of estrogen in the immune microenvironment of liver metastases. Nat Commun 2019;10:5745.
44. Farren MR, Sayegh L, Ware MB, Chen HR, Gong J, Liang Y, et al. Immunologic alterations in the pancreatic cancer microenvironment of patients treated with neoadjuvant chemo- and radiotherapy. JCI Insight 2020;5:e130362.
45. Brodt P. Role of the microenvironment in liver metastasis: from pre- to prometastatic niches. Clin Cancer Res 2016;22:5971–82.
46. Milette S, Sicklick JK, Lowy AM, Brodt P. Molecular pathways: targeting the microenvironment of liver metastases. Clin Cancer Res 2017;23:6390–9.
47. Vidal-Vanaclocha F. The prometastatic microenvironment of the liver. Cancer Microenviron 2008;1:113–29.
48. Friedman SL. Hepatic stellate cells: protean, multifunctional, and enigmatic cells of the liver. Physiol Rev 2008;88:125–72.
49. Yata Y, Scanga A, Gillan A, Yang L, Reif S, Breindl M, et al. DNase I-hypersensitive sites enhance alpha1(I) collagen gene expression in hepatic stellate cells. Hepatology 2003;37:267–76.
50. Bazhin AV, Shevchenko I, Umansky V, Werner J, Karakhanova S. Two immune faces of pancreatic adenocarcinoma: possible implication for immunotherapy. Cancer Immunol Immunother 2014;63:59–65.
51. Fukunaga A, Miyamoto M, Cho Y, Murakami S, Kawarada Y, Oshikiri T, et al. CD8+ tumor-infiltrating lymphocytes together with CD4+ tumor-infiltrating lymphocytes and dendritic cells improve the prognosis of patients with pancreatic adenocarcinoma. Pancreas 2004;28:e26–31.
52. Wormann SM, Diakopoulos KN, Lesina M, Algul H. The immune network in pancreatic cancer development and progression. Oncogene 2014;33:2956–67.
53. Costa-Silva B, Aiello NM, Ocean AJ, Singh S, Zhang H, Thakur BK, et al. Pancreatic cancer exosomes initiate pre-metastatic niche formation in the liver. Nat Cell Biol 2015;17:816–26.
54. Peinado H, Zhang H, Matei IR, Costa-Silva B, Hoshino A, Rodrigues G, et al. Pre-metastatic niches: organ-specific homes for metastases. Nat Rev Cancer 2017;17: 302–17.
55. Jamitzky S, Krueger AC, Janneschuetz S, Piepke S, Kailayangiri S, Spurny C, et al. Insulin-like growth factor-1 receptor (IGF-1R) inhibition promotes expansion of human NK cells which maintain their potent antitumor activity against Ewing sarcoma cells. Pediatr Blood Cancer 2015;62:1979–85.
56. Xu X, Mardell C, Xian CJ, Zola H, Read LC. Expression of functional insulin-like growth factor-1 receptor on lymphoid cell subsets of rats. Immunology 1995;85: 394–9.
57. Jiang H, Hegde S, Knolhoff BL, Zhu Y, Herndon JM, Meyer MA, et al. Targeting focal adhesion kinase renders pancreatic cancers responsive to checkpoint immunotherapy. Nat Med 2016;22:851–60.
58. Diana A, Wang LM, D'Costa Z, Allen P, Azad A, Silva MA, et al. Prognostic value, localization and correlation of PD-1/PD-L1, CD8 and FOXP3 with the desmoplastic stroma in pancreatic ductal adenocarcinoma. Oncotarget 2016; 7:40992–1004.
59. Connor AA, Denroche RE, Jang GH, Timms L, Kalimuthu SN, Selander I, et al. Association of distinct mutational signatures with correlates of increased immune activity in pancreatic ductal adenocarcinoma. JAMA Oncol 2017;3: 774–83.
60. Nosrati A, Tsai KK, Goldinger SM, Tumeh P, Grimes B, Loo K, et al. Evaluation of clinicopathological factors in PD-1 response: derivation and validation of a prediction scale for response to PD-1 monotherapy. Br J Cancer 2017;116: 1141–7.
61. Tumeh PC, Hellmann MD, Hamid O, Tsai KK, Loo KL, Gubens MA, et al. Liver metastasis and treatment outcome with anti-PD-1 monoclonal antibody in patients with melanoma and NSCLC. Cancer Immunol Res 2017;5:417–24.